Advanced structure methodologies for next-generation ground vehicles, Part 2: Case study

C. Pierre*, N. Vlahopoulos*, Z.D. Ma*, M.P. Castanier*, S.-Y. Lee*, A. Wang*,K.K. Choi[†], N.H. Kim[†] and J. Dong[†]

*University of Michigan, Ann Arbor, MI 48109 USA

[†]University of Iowa, 2222 Old Hwy 218 S, Iowa City IA 52242-1602, USA

Corresponding author, Z. D. Ma. Email address: mazd@umich.edu

Abstract: In the first paper of this two-part study basic theories were introduced for several new methodologies developed in the Automotive Research Center (a US Army TACOM Center of Excellence for Modelling and Simulation of Ground Vehicles at the University of Michigan) for the simulation and design of advanced structures and materials for next-generation ground vehicles. These new methodologies include: (1) an advanced topology optimisation technique for innovative conceptual design of vehicle structures and materials; (2) a systematic design optimisation process with efficient analysis and sensitivity analysis capabilities for detailed design modifications to improve the vibration and noise characteristics of a complex vehicle structure; (3) a reduced-order modelling technique that can be used to systematically generate low-order models for the prediction of vehicle vibration, power flow, and the effects of parameter uncertainties; and (4) an efficient and accurate energy boundary element analysis method for high-frequency noise analysis outside the vehicle. In this second paper, an extensive case study is presented to demonstrate how the methodologies presented in the first paper can be applied to a vehicle system. A pick-up truck equipped with an advanced hybrid propulsion system is considered in this paper, and various example design and prediction problems are discussed, which provide proof-of-concept for the methodologies developed.

Keywords: design optimisation, heavy vehicles, structural acoustics, topology optimisation.

1 Introduction – outline of the case study

One of major tasks at the ARC (Automotive Research Center, a US Army TACOM Center of Excellence for Modelling and Simulation of Ground Vehicles at the University of Michigan) is to develop new methodologies for advanced structures and materials for next-generation ground vehicles. Several major developments related to this task have been detailed in (Pierre *et al.*, 2004). First, an advanced topology optimisation technique has been developed, which provides extensive capabilities for laying out new, conceptually advanced designs for vehicle structures or substructures to achieve the goals of reduced weight and increased performance. Second, a 'sizing' design optimisation process has been developed for achieving detailed design modifications in order to improve the vibration and noise response of a complex vehicle structure. This development includes efficient analysis and sensitivity analysis capabilities for vibro-acoustic systems. Third, a component-based reduced order modelling technique has been developed for efficient vibration analysis. This technique has also been extended for analysing vibration transmission in a complex vehicle structural system to determine the power flow between components and to predict the effect of parameter uncertainties. Fourth, an energy boundary element analysis (EBEA) method has been developed for efficient and accurate high-frequency noise analysis, which extends the capability for predicting the acoustic field around the vehicle due to various sources.
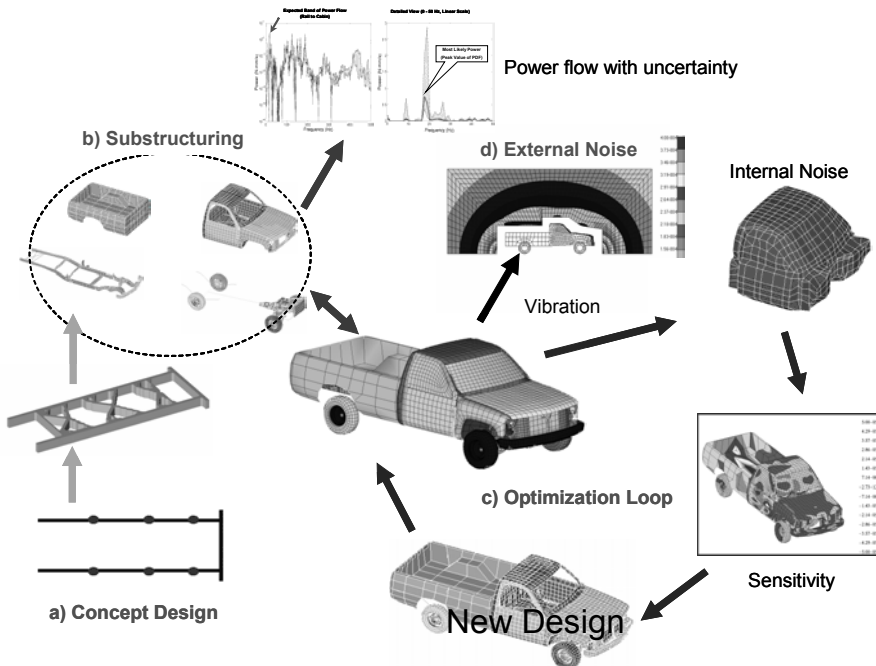

Figure 1 *A case study for the new methodologies developed.*

The overall objective of this paper is to demonstrate the methodologies developed in (Pierre *et al.*, 2004) through their application to a generic class-IIB truck. Figure 1 shows

a sketch of this case study, which illustrates how the new methodologies have been applied to the truck system for solving a number of example problems.

As shown in Figure 1(a), first the topology optimisation technique is applied to a concept design problem of a structural component in the truck. The chassis frame is selected as an example component to be redesigned in the case study. The reason for modifying this component is that the lateral vibration of the chassis frame has a major effect on the peak structure-borne noise that is transmitted inside the cabin to the location of the driver's ear. (This is discussed in more detail in Section 3.1.) Figure 1(b) shows that a reduced order modelling technique is then applied to the substructures in order to yield a low-order system model. The reduced order model can be used to efficiently predict the vibration response and to calculate the sensitivities for determining design changes in the optimisation process. Figure 1c shows that an integrated optimisation process is then applied to the structural-acoustic system for the objective considered in the case study. As shown in Figure 1(c), this optimisation process employs the vibration-noise prediction capabilities and sensitivity analysis method developed in (Pierre *et al.*, 2004). The design objective currently considered is to reduce the sound pressure level inside the cabin at the driver's ear position. Figure 1(b) also shows that the reduced order modelling technique can be used as a basis for predicting the power flow among the components as well as estimating the effect of parameter uncertainties on the response of the truck structure. Finally, Figure 1(d) shows that an energy boundary element analysis (EBEA) method is applied to predict high-frequency external noise, which extends the analysis capabilities for important vehicle characteristics such as radiated noise and acoustic signature.
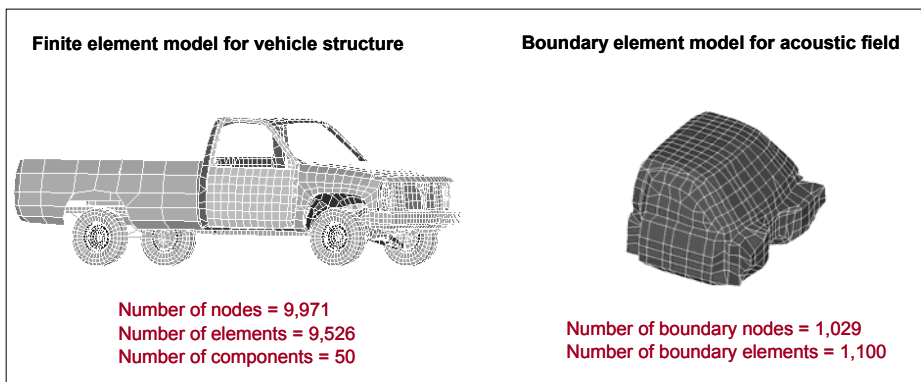

Finite element model for vehicle structure

Boundary element model for acoustic field

Number of nodes = 9,971
Number of elements = 9,526
Number of components = 50

Number of boundary nodes = 1,029
Number of boundary elements = 1,100

Figure 2 *Structural model and acoustic model used in the case studies.*

2   Dual-use truck system for the case study

A dual-purpose (military/commercial) concept truck is shown in Figure 2. In this paper, this truck is considered as an example structural-acoustic system, and it is used to demonstrate the new methodologies described in the first paper (Pierre *et al.*, 2004). The concept truck is powered by an advanced hybrid propulsion system, which includes hydraulic components for the regeneration of braking energy. The hydraulic pump in the

powertrain system provides an additional vibration excitation source to the vehicle structure. Because of this additional source of excitation, the vibration and noise levels of the truck are larger than for the same vehicle with a conventional powertrain. The current design goal is to reduce the vibration and noise by optimising the truck's structural design. In addition, the truck also needs to be optimised in order to reduce its total weight for achieving the aggressive fuel efficiency targets for an advanced hybrid vehicle. In the following examples, the methodologies presented in (Pierre *et al.*, 2004) are applied to this design problem in order to demonstrate how the new capabilities can be used to accomplish the design goals.

As shown in Figure 2, the concept truck structure is modelled by a finite element representation, which has 9971 nodes and 9526 finite elements. The truck model also contains 50 components (substructures). The acoustic field of the cabin cavity is modelled by a boundary element representation, which has 1029 boundary nodes and 1100 boundary elements.
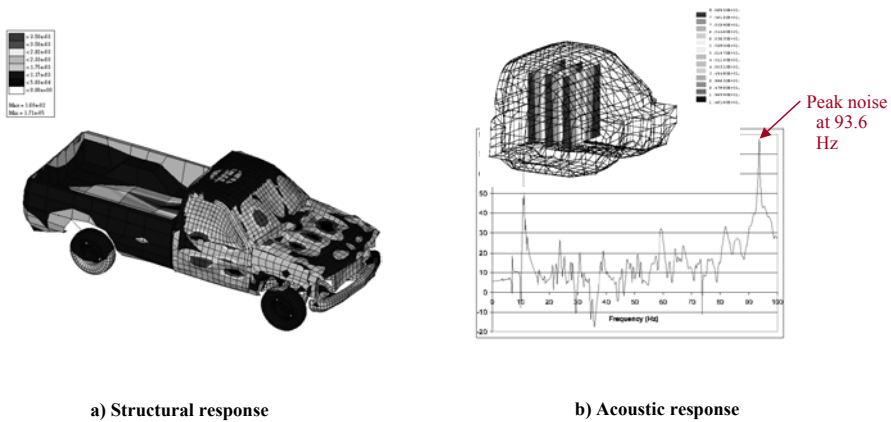

a) Structural response   b) Acoustic response

Figure 3   *Structural response and acoustic response of the structural-acoustic system.*

In the current design problem, the noise level inside the passenger compartment is chosen as the performance measure. The harmonic excitations at twelve locations are considered, which include four points at the spindles of the four wheels and eight mounting points of the powertrain and added hydraulic pump. Frequency response analysis is first carried out using MSC/NASTRAN for the nominal design to obtain the vibration response at a frequency range up to 100 Hz. Figure 3(a) shows an example result of the frequency response of the truck body at 93.6 Hz. An acoustic boundary element analysis is then carried out using the cabin acoustic boundary element model shown in Figure 2(b). Figure 3(b) shows the sound pressure level predicted at the driver's ear for the frequency range from 0 to 100 Hz and the sound pressure distribution at 93.6 Hz inside the cabin compartment. As shown in Figure 3(b), the maximum sound pressure level at the driver's ear is at 93.6 Hz with an amplitude of 77.8 dB when the reference pressure of 2×10^{-8} kg/mm·s^2 is used. (Note that the responses shown in this paper have been normalised with respect to the excitations.)

3   Example results

3.1   Topology optimisation of a simplified model of the chassis frame

This first example illustrates how the topology optimisation technique can be utilised to redesign the chassis frame structure (Ma *et al.*, 2002). As shown in Figure 4, from a previous study using sensitivity analysis, the peak noise at 93.6 Hz heard by the driver is mainly due to the first in-plane mode of the chassis frame. Therefore, this part of the investigation is focused on how the topology optimisation technique can be applied to redesign the chassis frame in order to improve its vibration performance. The first objective is to maximise the first in-plane eigenfrequency of the frame. Figures 5 and 6 depict preliminary research results obtained by considering a simplified yet representative two-dimensional model of the frame. In this design problem, it is assumed that the rails and the bumper cannot be changed at the design stage; these are shown as the blue areas in Figure 5(a). Only the connectors between the two rails were sought in the design problem in order to maximise the eigenfrequency of the first in-plane mode of the frame.
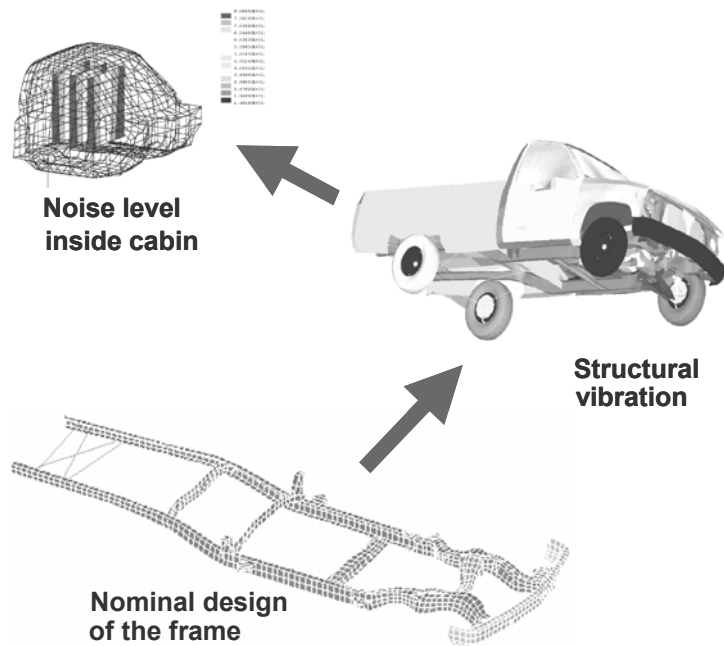

Figure 4   *Frame vibration-induced peak noise in the structural-acoustic system.*

a) Design definition
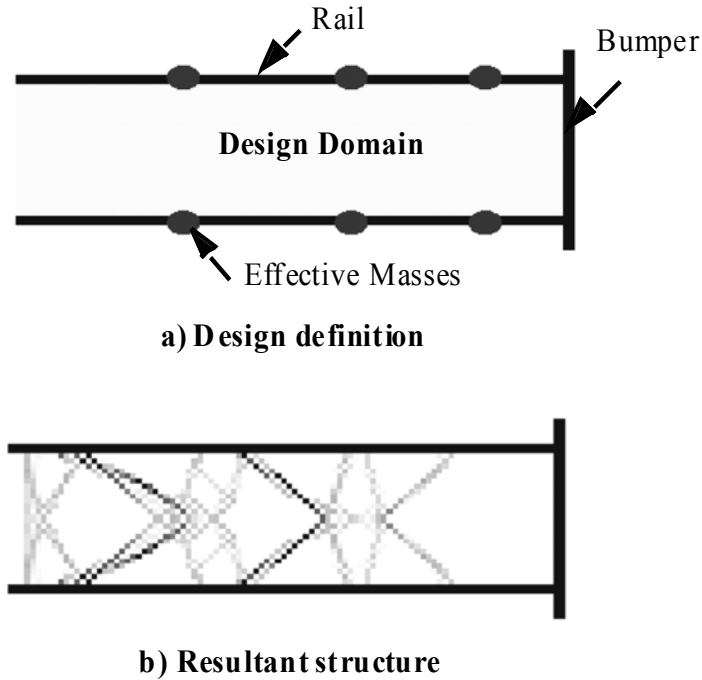

b) Resultant structure

Figure 5 *Single-domain topology optimisation.*

As a first try, a single-domain topology optimisation was conducted, in which the connectors are allowed to be placed anywhere in the design domain between the two rails (Figure 5(a)), with a constraint on the total amount of the material for building the connectors. The optimisation problem for this design can be written as

$$
\begin{aligned}
& \text{Maximize } \lambda_1(\mathbf{X}) \\
& \text{Subject to} : h(\mathbf{X}) \leq 0 \\
& \qquad\qquad \underline{x}_j \leq x_j \leq \overline{x}_j \quad (j = 1, 2, ..., n) \\
& \text{and} \qquad (\mathbf{K} - \lambda_1 \mathbf{M})\boldsymbol{\phi}_1 = 0
\end{aligned}
\tag{1}
$$

where λ_1 denotes the first eigenvalue of chassis frame structure; h denotes the constraint function for the total area (since we are considering a two-dimensional design problem) of the connector structure in the design domain shown in Figure 5(a); $\mathbf{X} = \{x_1, x_2, ..., x_n\}^T$ denotes the vector of the design variables defined in (Pierre *et al.*, 2004); $\underline{x}_j$ and $\overline{x}_j$ denote the lower and upper bounds of design variable x_j, respectively; $\mathbf{M}$ and $\mathbf{K}$ denote the mass and stiffness matrices of the chassis frame based on a finite element discretisation, and $\boldsymbol{\phi}_1$ is the first eigenvector of the chassis frame. Figure 5(b) shows the result obtained from the optimisation process (1). It is seen that the resultant design may not be the desired one because of the complicated geometry of the connectors' design, which may be too difficult to fabricate. Also, the resultant design provides no support in the front part of the frame, which might be desired in a real vehicle system. This undesired design might be due to the lack of several considerations in the design process,

for example, the out-of-plane loads and more accurate boundary conditions and loading conditions. However, it would be difficult to account for all such factors (e.g. accurate boundary conditions and loading conditions for the design problem) in the numerical process because these are dependent on the wide variety of operating conditions of the vehicle.
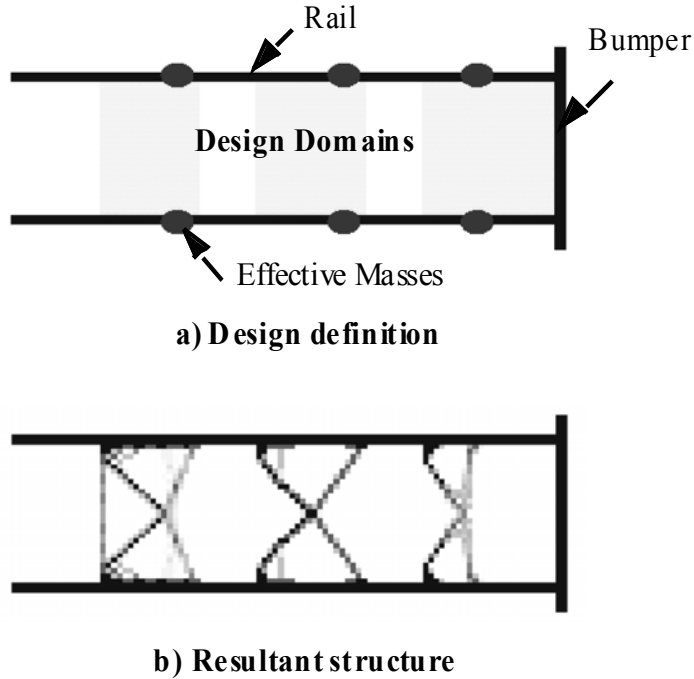

a) Design definition

b) Resultant structure

Figure 6   *Multi-domain topology optimisation.*

In a second try, a multi-domain topology optimisation introduced in (Pierre *et al.*, 2004) was conducted. This design process limited the design space for each connector and assigned a specific amount of the material to each individual connector. Yellow areas in Figure 6(a) indicate the allowable locations for the connectors. The multi-domain topology optimisation problem can be then written as

$$
\begin{aligned}
&\text{Maximize } \lambda_1(\mathbf{X}) \\
&\text{Subject to}: h_j(\mathbf{X}) \le 0 \quad (j = 1,2,...,m) \\
&\qquad \underline{x}_j \le x_j \le \overline{x}_j \quad (j = 1, 2, ..., n) \\
&\text{and} \qquad (\mathbf{K} - \lambda_1 \mathbf{M})\boldsymbol{\phi}_1 = 0
\end{aligned}
\tag{2}
$$

where h_j denotes the j-th constraint function for the total area of the j-th connector in the j-th subdomain shown in Figure 6(a) (where j = 1, 2, …, m, and m=3). The optimisation algorithm, GSAO, presented in (Pierre *et al.*, 2004) has been used to solve the optimisation problem (2) with the use of the updating rule 3 (i.e., Equation 5 in (Pierre *et al.*, 2004)). As shown in Figure 6(b), a more reasonable design was obtained because the designer had more control over the result by using a multi-domain topology optimisation technique. Figure 7 further illustrates the finalised shape of the design obtained in Figure 6(a), which can be used effectively for the manufacturing process. Table 1 illustrates the

comparison of the optimum design obtained through the topology optimisation process with a nominal design shown in Figure 8, which is made with the same amount of the material. As shown in Table 1, using the optimisation process has doubled the fundamental eigenfrequency.
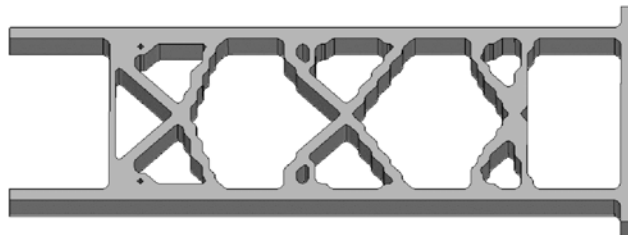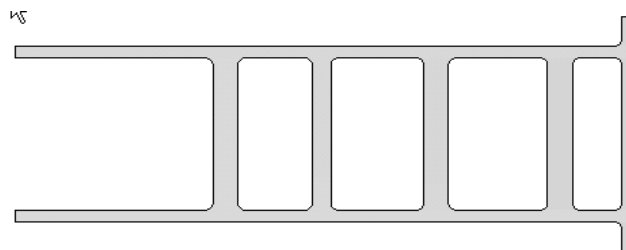

Figure 7 *Finalised design of Figure 6(a).*

Figure 8 *A nominal design for comparison purposes.*

Table 1 Comparison of nominal design and optimum design for normalised eigenfrequencies.

Mode number	Nominal design	Optimum design
1	2.99	6.40
2	13.4	20.3
3	28.5	31.0

Note that other objective functions could also be considered in the design problem: maximising the distances between the eigenfrequencies of the frame and the excitation frequencies, minimising the distances between the eigenfrequencies and the desired frequencies, and so forth (Ma, *et al.*, 1994; Ma, *et al.*, 1995a; Ma, *et al.*, 1995b). For example, for the design problem mentioned before, suppose that the chassis frame shown in Figure 7 has specific target values for the first three eigenfrequencies: $f_1^* = 5$ Hz, $f_2^* = 20$ Hz, and $f_3^* = 35$ Hz. In this case, a multi-domain topology optimisation problem can be stated as follows:

$$\text{Minimize } f(\mathbf{X}) = \sum_{k=1}^{3} \frac{1}{(\lambda_k^*)^2} w_k (\lambda_k - \lambda_k^*)^2$$

$$\text{Subject to}: h_j(\mathbf{X}) \leq 0 \quad (j = 1, 2, ..., m) \tag{3}$$

$$\underline{x}_j \leq x_j \leq \overline{x}_j \quad (j = 1, 2, ..., n)$$

$$\text{and} \quad (\mathbf{K} - \lambda_k \mathbf{M})\boldsymbol{\phi}_k = 0 \quad (k = 1, 2, 3)$$

where $\lambda_k^* = (2\pi f_k^*)^2$ $(k = 1, 2, 3)$, and w_k $(k = 1, 2, 3)$ are weighting factors. Figure 9(a) shows the optimum structure obtained through applying the topology optimisation process to the design problem of Equation (3). As shown in Figure 9(a), the optimum structure obtained here has a topology that is quite different from that obtained from the previous optimisation process of Equation (2). A table shown in Figure 9(b) compares the obtained eigenfrequencies with the desired ones. It is seen that the maximum difference between the obtained and desired values is less than 11% for these three eigenfrequencies. Furthermore, Figure 9(c) shows a scaled prototype fabricated for this design using a rapid prototyping machine. Note that additional manufacturing constraints must be considered in the design process so that the fabrication cost can be minimised for a given manufacturing process. Also note that, for a realistic engineering design, the topology optimisation process presented in this paper needs to be extended with the capability to distribute the material in a three-dimensional domain. This three-dimensional topology optimisation is under development and will be the subject of future work.
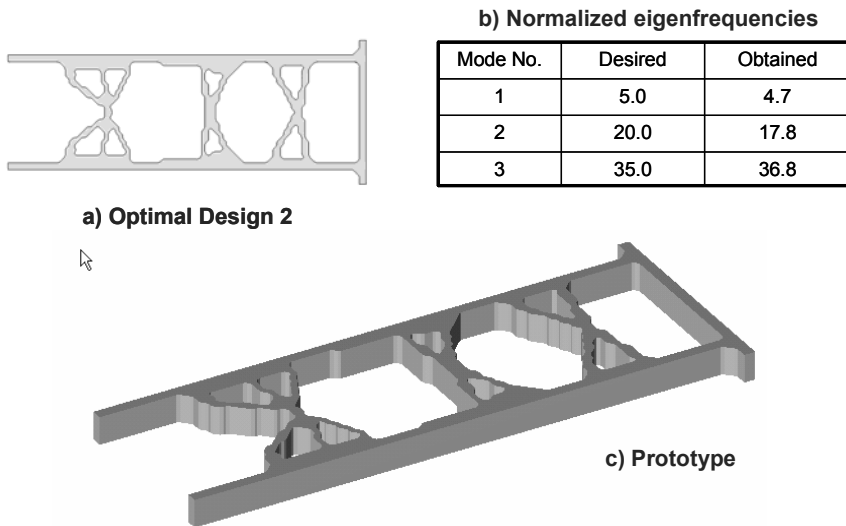
b) Normalized eigenfrequencies

Mode No.	Desired	Obtained
1	5.0	4.7
2	20.0	17.8
3	35.0	36.8

a) Optimal Design 2

c) Prototype

Figure 9   *Topology optimisation for desired eigenfrequencies.*

3.2   *Design sensitivity analysis and optimisation of the truck structure system*

This second example illustrates how the design sensitivity method developed in (Pierre *et al.*, 2004) can be applied to the truck re-design problem when the truck is considered as a vibro-acoustic system (Kim, *et al.*, 2003). In this example problem, the noise level of the passenger compartment is chosen as the performance measure, and panel thicknesses of the components are chosen as the design variables. The predicted sound pressure levels at the driver's ear position for the nominal design are shown in Table 2 for the selected eight frequencies. As shown in Table 2, the sound pressure level at 93.6 Hz is significantly higher than at other frequencies, design optimisation is therefore carried out at that frequency.

Table 2   Sound pressure levels at driver's ear position.

Frequency (Hz)	Pressure (kg/mm·sec^2)	Phase angle (degree)
47.3	0.64275E–04	66.915
59.5	0.35889E–03	328.99
75.9	0.66052E–04	193.91
81.8	0.41081E–03	264.21
86.0	0.21629E–03	176.18
90.5	0.43862E–03	171.44
93.6	0.75627E–02	178.30
98.7	0.22676E–03	226.07

Forty design variables are selected in this example design problem. First, the acoustic adjoint problem defined in Equation (11) of (Pierre *et al.*, 2004), namely

$$\mathbf{A}^T \boldsymbol{\eta} = \mathbf{e} \tag{4}$$

is solved, and then the structural adjoint problem defined in Equation (15) of (Pierre *et al.*, 2004), namely

$$\left(j\omega \mathbf{M} + \kappa \mathbf{K} \right) \boldsymbol{\lambda}^* = \mathbf{L} \tag{5}$$

is solved to obtain the adjoint response $\boldsymbol{\lambda}$, where, $\mathbf{L} = \mathbf{b} + \mathbf{B}^T \boldsymbol{\eta}$ stands for the *adjoint load*. Using the velocity response $\mathbf{v}$, adjoint response $\boldsymbol{\lambda}$, and the numerical integration process given in Equation (18) of (Pierre *et al.*, 2004), the sensitivities for each structural panel can be calculated, which are shown in Table 3 at the initial design point. Since the numerical integration process is carried out on each finite element, the element sensitivity information can be also calculated without additional effort. Figure 10(a) shows the sensitivity contributions of major components to the sound pressure level, while Figure 10(b) shows the sensitivity contribution of the each element to the sound pressure level. This type of graphics-based sensitivity information is very helpful for the design engineer to determine the direction of the design modification.

Table 3   Normalised sound pressure level sensitivity w.r.t. panel thickness.

Component	Sensitivity	Component	Sensitivity
Chassis	−1.0	Chassis MTG	−0.11
Left wheelhouse	−0.82	Chassis connectors	−0.10
Right door	0.73	Right fender	−0.07
Cabin	−0.35	Left door	−0.06
Right wheelhouse	−0.25	Bumper	−0.03
Bed	−0.19	Rear glass	0.03

Frequency = 94 *Hz*
Design parameters:
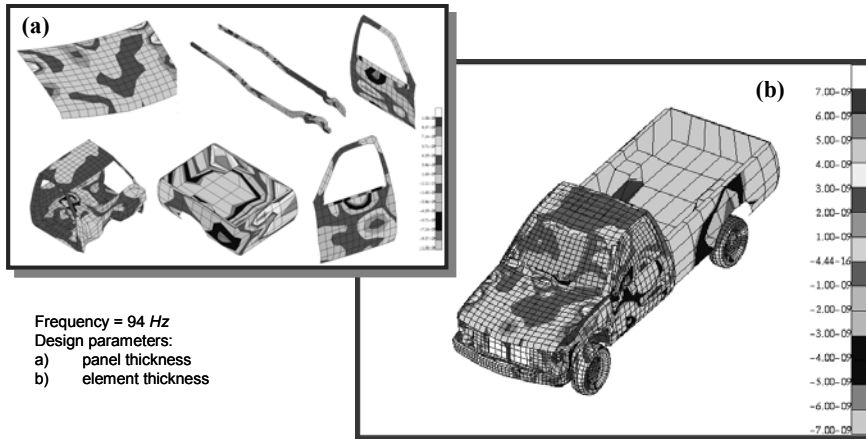a)   panel thickness
b)   element thickness

Figure 10 *Panel and element design sensitivity w.r.t. panel thickness.*

Table 4   Comparison of the new design sensitivity analysis (DSA) method with the finite difference method (FDM).

Design	Perturbed	FDM	DSA	Ratio (%)
Bumper	.40292	−3.5739E−3	−3.9091E−3	91.43
Chassis	.40196	−3.1287E−1	−3.0824E−1	101.50
Arm LL	.40288	−9.8022E−3	−9.6368E−3	101.72
Arm LR	.40250	−9.0502E−2	−9.6967E−2	93.33
Oil box	.40293	1.9519E−3	2.0538E−3	95.04
Brake FL	.40289	−6.9373E−3	−6.4794E−3	107.07
Brake FR	.40239	−1.0890E−1	−9.7718E−2	111.45
Chassis conn	.40274	−5.2836E−2	−5.2732E−2	100.20
Arm conn UL	.40293	−4.1533E−5	−4.1283E−5	100.60
Arm conn UR	.40293	−1.1367E−5	−1.0735E−5	105.89

In Table 4, the accuracy of the sensitivity results obtained by the new method are compared to the sensitivity results calculated using the finite difference method for the design variables that have the highest values. In this case, the vertical velocity at the center of the cabin roof is considered as a performance measure. It is seen that the proposed sensitivity results agree with the finite difference sensitivity results within a range of 10% when the panel thicknesses are perturbed by 0.1%.
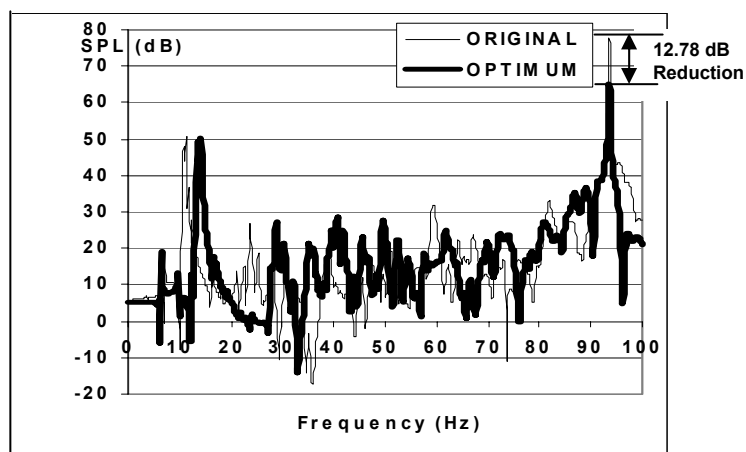

Figure 11 *Sound pressure level frequency response at driver's position (initial design and optimum design).*

Table 5   *Initial and optimum design result.*

Design variable	Initial design	Optimum design
x_1 (Chassis)	3.137	1.568500
x_2 (Fender-left)	0.800	0.400200
x_3 (Fender-right)	0.800	0.400200
x_4 (Wheelhouse-left)	0.696	0.348000
x_5 (Wheelhouse-right)	0.696	0.368218
x_6 (Cabin)	2.500	1.250080
x_7 (Door-left)	1.240	1.859970
x_8 (Door-right)	1.240	0.620000
x_9 (Chassis -conn)	3.611	1.805500
x_{10} (Chassis -MTG)	3.000	1.500000

Finally, an optimisation process is applied to the truck structure to minimise the vehicle weight while reducing the peak noise level at driver's ear position from 77.8 dB to 65.0 dB, which is a 77% reduction in magnitude. Ten design variables are selected to change during design optimisation, including the panel thicknesses of chassis, fenders, wheelhouses, cabin, doors, etc, which do not largely affect other system performance measure but significantly influence the sound and vibration level inside the cabin.

Figure 11 shows the final result obtained from this optimisation process and compares the new result with the nominal result, where the peak sound pressure has been reduced from 77.8 dB to 65.0 dB. Table 5 further illustrates the design changes for the ten selected panel thicknesses, which result in a reduction of 178 Kg in the total vehicle weight.

3.3   *Power flow and structural uncertainty analysis*

To study the effect of design uncertainty with an efficient computational approach, the reduced-order model presented earlier is used to perform a power flow analysis that characterises the vibration response of the system in a concise manner. The equations of motion can be written as

$$\overline{z}_b(\omega;\boldsymbol{\theta})\overline{v}_b(\omega;\boldsymbol{\theta}) = \overline{f}_b(\omega;\boldsymbol{\theta}) \qquad for \quad b = 1, 2, \cdots n^{ROM} \tag{6}$$

where θ is the random variable set and $\overline{z}_b$ is the diagonal element of the impedance matrix $\overline{\mathbf{Z}}$.

$$\overline{\mathbf{Z}} = j\omega\overline{\mathbf{M}} + \kappa\overline{\mathbf{K}} \tag{7}$$

Then, a locally linear interpolation (LLI) of the modal velocities and modal matrix elements can be constructed with a set of piecewise linear functions over the random variable (r.v.) domain (Tan, *et al.*, 2001). This results in a finite-element-like discretisation over the r.v. domain. It is assumed that Ω is the r.v. domain that consists of subdomains Ω^e, such that $\Omega = \bigcup_{e=1}^{n^E} \Omega^e$, where n^E indicates the number of elements that constitute the entire r.v. domain. It is also assumed that the magnitude and the unwrapped phase of the modal velocity can be approximated by a set of piecewise linear functions over the r.v. domain. The linear approximation of the magnitude and phase of the modal velocity will be

$$\left|\overline{v}_b(\omega;\boldsymbol{\theta})\right| = \mathbf{N}(\boldsymbol{\theta})\mathbf{a}_b(\omega) = \sum_{e=1}^{n^E} \mathbf{N}^e(\xi)\mathbf{a}_b^e(\omega),$$

$$\arg\!\left(\overline{v}_b(\omega;\boldsymbol{\theta})\right) = \mathbf{N}(\boldsymbol{\theta})\mathbf{c}_b(\omega) = \sum_{e=1}^{n^E} \mathbf{N}^e(\xi)\mathbf{c}_b^e(\omega) \tag{8}$$

where $N(\theta)$ is the global shape function, while $N^e(\xi)$ is the local shape function with ξ representing the local coordinates. Then, the equations of motion can be cast into the weak formulation for the magnitude and phase of modal velocity:

$$\int_\Omega w \cdot \left|\overline{z}_b(\omega;\boldsymbol{\theta})\right| \cdot \left|\overline{v}_b(\omega;\boldsymbol{\theta})\right| d\Omega = \int_\Omega w \cdot \left|\overline{f}_b(\omega;\boldsymbol{\theta})\right| d\Omega \tag{9}$$

$$\int_\Omega w \cdot \left[\arg\!\left(\overline{z}_b(\omega;\boldsymbol{\theta})\right) + \arg\!\left(\overline{v}_b(\omega;\boldsymbol{\theta})\right)\right] d\Omega = \int_\Omega w \cdot \arg\!\left(\overline{f}_b(\omega;\boldsymbol{\theta})\right) d\Omega \tag{10}$$

Substituting the linear approximation of the magnitude and phase of the modal velocity, and applying Galerkin's method for the weighting function, w, yields the modal velocity approximated by a piecewise linear function over the r.v. domain. This

interpolation of the modal velocity can then be used to approximate the distribution of the power flow over the r.v. domain.

At this point, various statistical quantities of the power flow can be calculated. The ensemble-averaged power flow is found as

$$E_\theta\left[\Pi_i\left(\omega;\boldsymbol{\theta}\right)\right] = \frac{1}{2}\sum_{b=1}^{n^{ROM}}\mathrm{Re}\left[\int_\Omega pdf_{in}\left(\boldsymbol{\theta}\right)\overline{f}_{ib}\left(\omega;\boldsymbol{\theta}\right)^* \overline{v}_b\left(\omega;\boldsymbol{\theta}\right)d\Omega\right]$$

$$-\frac{1}{2}\sum_{b=1}^{n^{ROM}}\sum_{c=1}^{n^{ROM}}\int_\Omega pdf_{in}\left(\boldsymbol{\theta}\right)\overline{v}_b\left(\omega;\boldsymbol{\theta}\right)^* \overline{C}_{ibc}\left(\omega;\boldsymbol{\theta}\right)\overline{v}_c\left(\omega;\boldsymbol{\theta}\right)d\Omega \tag{11}$$

where $pdf_{in}(\theta)$ is the joint probability density function of random variable set θ. Furthermore, the cumulative distribution function (CDF) and the probability density function (PDF) of the power flow can be determined. Given the joint PDF of the random variable set θ (input), the CDF of the power flow (output) can be expressed as

$$cdf_{out}\left(\pi_i\right) = \iint\cdots\int_{\Pi_i \leq \pi_i} pdf_{in}\left(\boldsymbol{\theta}\right)d\boldsymbol{\theta} \tag{12}$$

where the variable π_i represents a value taken by $\Pi_i(\boldsymbol{\theta})$. Then, the PDF of the power flow can be formulated as

$$pdf_{out}\left(\pi_i\right) \approx \iint\cdots\int_{\pi_i < \Pi_i \leq \pi_i+\Delta\pi_i} pdf_{in}\left(\boldsymbol{\theta}\right)d\boldsymbol{\theta}\frac{1}{\Delta\pi_i} \tag{13}$$

Using the LLI approximation of the power flow over the r.v. domain, the multiple integrals of Equations (12) and (13) can be solved numerically, yielding the CDF and PDF of the power flow.

As an example case, the effects of parameter uncertainties in the front and rear cabin mounts are considered, as shown in Figure 12. The mounting stiffnesses are assumed to have +/- 20% variation about the nominal values of 1350 N/mm (*x*, *y* directions) and 1230 N/mm (z direction) with two independent, uniform PDFs. Figure 13 shows the expected band of power flow from the rail to the cabin for the given variation of mounting stiffnesses, obtained from the power flow approximated by the LLI method over the r.v. domain. In Figure 13, the largest difference between the upper and lower bounds of the power flow occurs at 18.9 Hz. For this frequency, Figure 14 shows the CDF from a Monte Carlo simulation with 2,000 realisations, as well as the CDFs from the LLI method employing 8x8 elements and 12 × 12 elements over the r.v. domain. With this discretisation of the r.v. domain, the LLI method provides a good approximation relative to the Monte Carlo simulation. Figure 14 also shows a good agreement between the histogram obtained from the Monte Carlo results and the PDF calculated with the LLI method. Both sets of results indicate that there is a significant difference between the most likely value of power flow, which corresponds to the peak of the PDF, and the ensemble-averaged value, which is denoted by the vertical line. For

further illustration of the response statistics, Figure 15 shows the 95th, 50th, and 5th percentiles of the power flow.
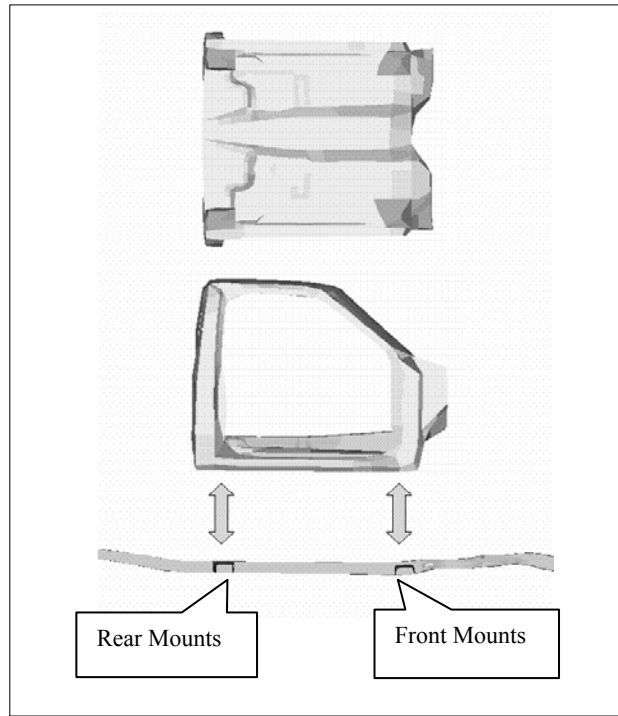

Figure 12 *Schematic display showing the connection of mounting stiffnesses (r.v.).*
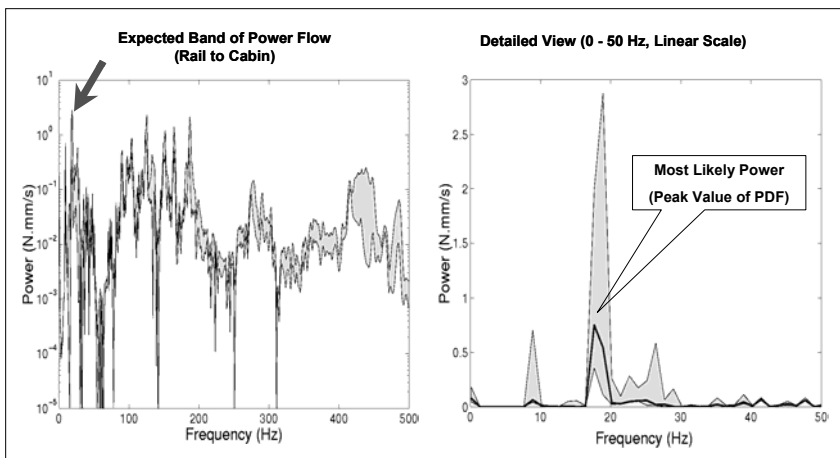

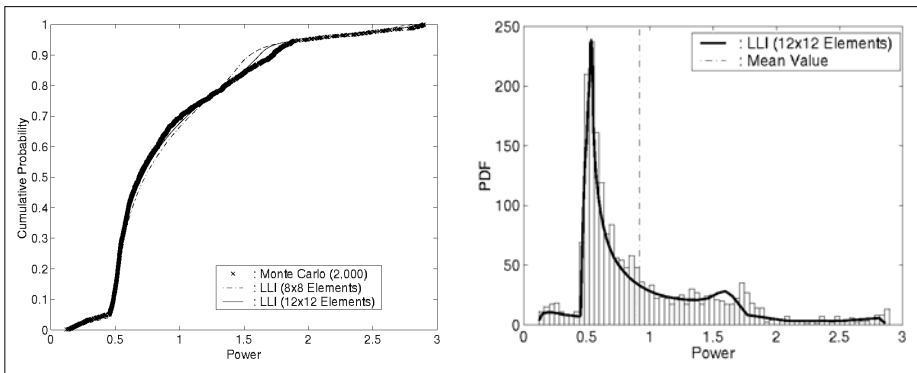**Figure 13** *Expected band of power flow from rail to cabin.*

Figure 14 *Comparison of cumulative probabilities and probability density functions predicted by Moute Carlo simulation and LLI.*
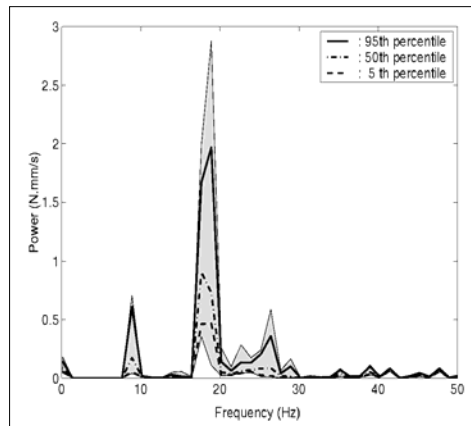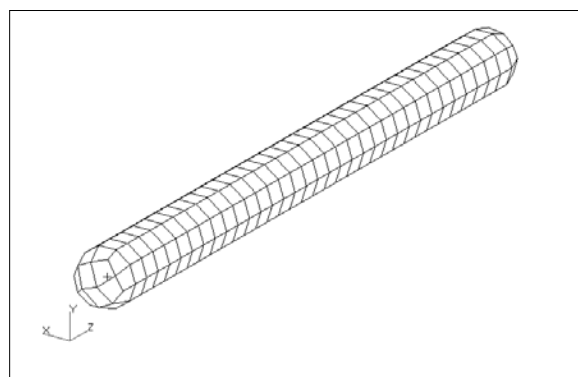

Figure 15 *5th, 50th, and 95th percentile power flow.*

Figure 16 *EBEA model for the cylindrical structure.*

(a) Calculated by EBEA   **(b) Calculated by analytical solution**
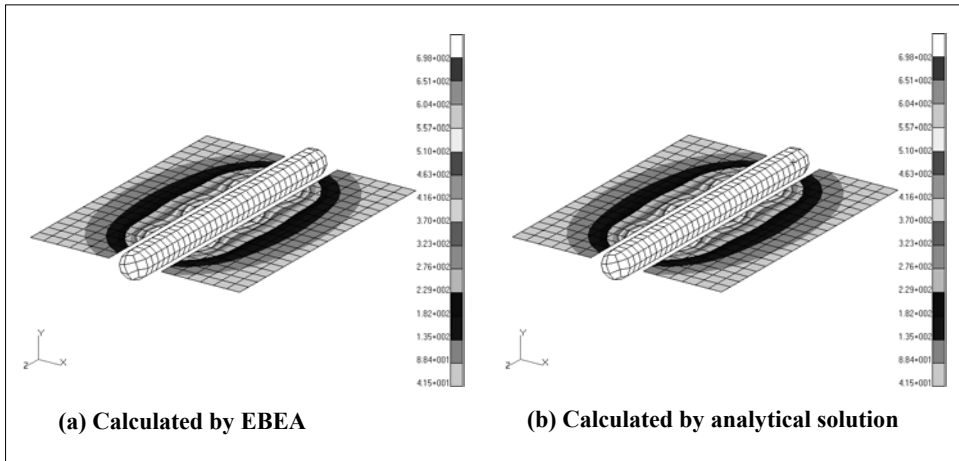
Figure 17 *Distribution of the acoustic energy density in the field.*

(a) Calculated by EBEA   **(b) Calculated by analytical solution**
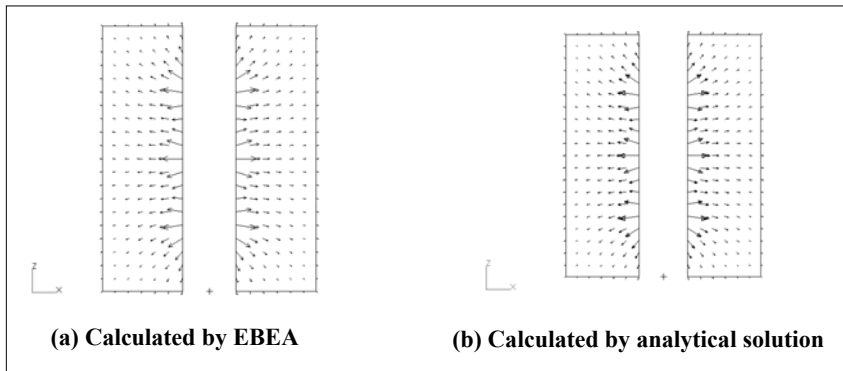
Figure 18 *Acoustic energy intensity vector in the field.*

3.4   Energy boundary element analysis (EBEA).

To demonstrate the validity of the EBEA formulation and its implementation (Pierre *et al.*, 2004), numerical results are compared with the analytical solutions. The acoustic medium used in the following examples is water, with density of 1000 kg/m^3, and speed of sound equal to 1500 m/s. Computations are performed at the centre frequency for the 3000 Hz 1/3 octave band. A cylindrical radiator with two end caps is analysed. The EBEA model for the cylinder is depicted in Figure 16. The analytical solution is generated by placing three incoherent point sources of unit strength along the axis of the cylinder. The surface of the cylinder is considered as transparent during the analytical computations. The acoustic intensity is computed on the cylinder surface and results for the acoustic energy density and intensity are also computed at field points. The acoustic intensity on the surface of the transparent cylinder is utilised as the boundary condition for the EBEA analysis. A distribution of energy sources and energy sinks is computed

first on the surface of the model, and then results are computed at the field points. Since the intensity boundary conditions of the EBEA analysis were evaluated from the analytical solution, it is expected that the EBEA results at the field points will correlate with the analytical results. Results for the acoustic energy density at the field points are illustrated in Figure 17 for the EBEA results (18(a)) and for the analytical solution (18(b)) respectively. Results for the acoustic intensity computed by the two methods are illustrated in Figure 18. The EBEA formulation is valid only for unbound medium. Since the energy sources which comprise the primary variables of the EBEA formulation originate from monopoles either in the free field or in the presence of a half space, the EBEA solution is not suitable for interior high frequency acoustic computations. Instead, an EFEA analysis that uses acoustic energy finite elements can be employed for high frequency acoustic computations (Zhang *et al.*, 2002).
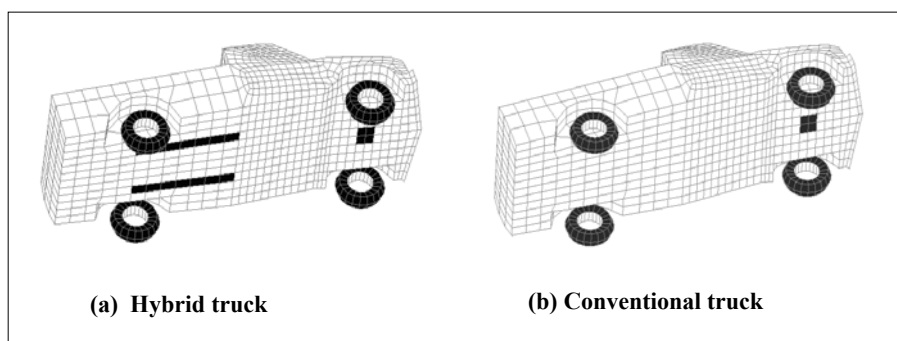

(a) **Hybrid truck**   (b) **Conventional truck**

Figure 19 *Excitation on the vehicle.*

As an engineering application for the case study, the acoustic field around the truck is evaluated. Excitations representing a conventional powertrain, the tyres, and the hydraulic components of a hydraulic hybrid powertrain are considered in the EBEA computations. In this case study a unit intensity boundary condition is applied on the parts of the model that represent the noise sources. Acoustic intensity test data, which are measured in the vicinity of actual noise sources, can be used as intensity boundary conditions in a practical prediction. In this case study the acoustic field in the vicinity of the vehicle is computed for the set of sources that represent both the conventional and the hybrid powertrain. Figure 19 shows the excitation locations as shaded areas where non-zero intensity boundary conditions are applied on the EBEA model of the truck for the hydraulic hybrid powertrain (Figure 19(a)) and for the conventional powertrain (Figure 19(b)). Typical results from both analyses are illustrated in Figure 20(a)-(e) for an excitation frequency of 1000 Hz. As expected, the acoustic field from the hydraulic hybrid presents higher noise levels around the vehicle. The acoustic field computed around the passenger cabin can be readily utilised as the excitation for a high-frequency air-borne interior acoustic analysis. The EBEA constitutes the only high-frequency method that can propagate the noise from the source to the acoustic space around the vehicle in high-frequency air-borne noise applications. The acoustic field computed around the vehicle by the EBEA can constitute the excitation for a SEA interior airborne noise analysis (Wang *et al.*, 1999).
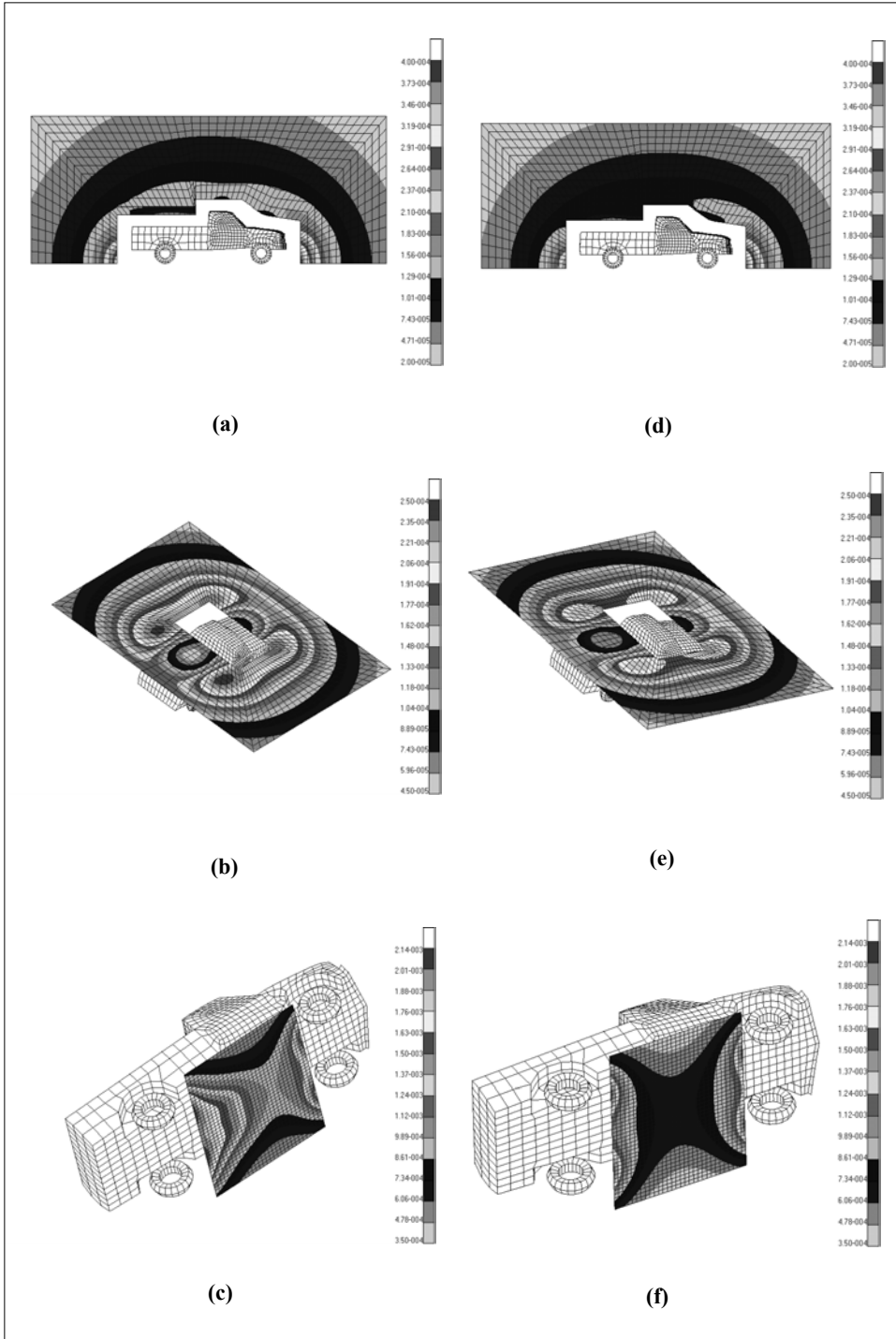
Figure 20 *Acoustic energy density predicted for: (a)-(c) Hybrid truck, (d)-(f): Conventional truck.*

4 Conclusions

In this second paper of a two-part study, the new methodologies presented in the first paper were applied to a generic truck structural system in order to demonstrate their feasibility. Several example problems were discussed, which include:

1   the topology optimisation for a simplified model of the truck chassis frame,

2   a size design optimisation of the vibro-acoustic system using the advanced prediction and sensitivity analysis methods,

3   power flow and structural uncertainty analysis based on the reduced-order modelling technique, and

4   external noise prediction using the energy boundary element method.

Based on this case study, it is seen that the new methodologies can be applied to a wide range of design problems, and they can be used effectively to simulate and optimise the dynamic response of the structural design, thus significantly improving the structural performance of an automotive vehicle system.

Acknowledgements

References

Kim, N.H., Dong J., Choi, K.K., Vlahopoulos, N., Ma, Z.-D., Castanier, M. and Pierre, C. (2003) 'Design sensitivity analysis for a sequential structural-acoustic problem', *Journal of Sound and Vibration*, Vol. 263, No. 3, pp. 569-591.

Ma, Z.D., Kikuchi, N. and Cheng, H.-C. (1995b) 'Topological design for vibrating structures', *Comput. Methods. Mech. Energ.*, Vol. 121, pp. 259-280.

Ma, Z.D., Kikuchi, N., Cheng, H.-C. and Hagiwara, I. (1994) 'Structural design for obtaining desired frequencies by using the topology and shape optimisation method', *Computing System in Engineering*, Vol. 5, No. 1, pp. 77-89.

Ma, Z.D., Kikuchi, N., Cheng, H.-C. and Hagiwara, I. (1995a) 'Topological optimisation technique for free vibration problems', *ASME Journal of Applied Mechanics*, Vol. 62, pp. 200-207.

Ma, Z.D., Kikuchi, N., Pierre, C. and Raju, B. (2002) 'Multi-domain topology optimisation for vehicle substructure design', *Proceedings of 2002 ASME International Mechanical Engineering Congress and Exposition*, November 17-22, New Orleans, Louisiana.

Pierre, C., Vlahopoulos, N., Ma, Z.D., Castanier, M.P., Lee, S.-Y., Wang, A., Choi, K.K., Kim, N.H. and Dong, J. (2004) 'Advanced structure methodologies for next-generation ground vehicles, Part 1: Basic theories', *Int. J. Heavy Vehicle Systems*, Vol. 11, Nos 3/4, pp. 257-281.

Tan, Y.C., Castanier, M.P. and Pierre, C. (2001) 'Statistical approximations for characteristic-mode-based power flow analysis', *Proceedings of the 42nd AIAA/ASME/ASCE/AHS/ASC Structures, Structural Dynamics, and Materials Conference and Exhibit*, April 16–19, Seattle, WA.

Wang, D., Goetchius, G. M. and Onsay, T. (1999) 'Validation of a SEA model for a minivan: use of ideal air- and structure- borne sources', SAE Noise and Vibration Conference, Traverse City, May, SAE Paper 1999-01-1697, pp. 381-388.

Zhang, W. Wang, A. and Vlahopoulos, N. (2002) 'An alternative energy finite element formulation based on incoherent orthogonal waves and its validation for marine structures', *Finite Elements in Analysis and Design*, Vol. 38, pp. 1095-1113.